MNRAS **000**, 1–?? (2019) Preprint 17 April 2019 Compiled using MNRAS LATEX style file v3.0

Nebular Line Emission During the Epoch of Reionization

Stephen M. Wilkins,[1⋆] Christopher C. Lovell,[1] Ciaran Fairhurst,[1] Yu Feng,[2] Tiziana Di Matteo,[3,4] Rupert Croft,[3,4] Jussi Kuusisto,[1] Aswin P. Vijayan,[1] Peter Thomas,[1]

[1] *Astronomy Centre, Department of Physics and Astronomy, University of Sussex, Brighton, BN1 9QH, UK*
[3] *Berkeley Center for Cosmological Physics, University of California, Berkeley, Berkeley CA, 94720, USA*
[2] *McWilliams Center for Cosmology, Carnegie Mellon University, Pittsburgh PA, 15213, USA*
[4] *School of Physics, University of Melbourne, VIC 3010, Australia.*

Accepted XXX. Received YYY; in original form ZZZ

ABSTRACT

Nebular emission lines associated with galactic HII regions carry information about both physical properties of the ionised gas and the source of ionising photons as well as providing the opportunity of measuring accurate redshifts and thus distances once a cosmological model is assumed. While nebular line emission has been extensively studied at lower redshift there are currently only few constraints within the epoch of reionisation (EoR, $z > 6$), chiefly due to the lack of sensitive near-IR spectrographs. However, this will soon change with the arrival of the *Webb Telescope* providing sensitive near-IR spectroscopy covering the rest-frame UV and optical emission of galaxies in the EoR. In anticipation of *Webb* we combine the large cosmological hydrodynamical simulation BlueTides with photoionisation modelling to predict the nebular emission line properties of galaxies at $z = 8 \rightarrow 13$. We find good agreement with the, albeit limited, existing direct and indirect observational constraints on equivalent widths though poorer agreement with luminosity function constraints. We also find that the predicted Hα - star formation rate calibration differs significantly from commonly assumed values.

Key words: galaxies: high-redshift – galaxies: photometry – methods: numerical – galaxies: luminosity function, mass function

1 INTRODUCTION

Massive stars and active galactic nuclei (AGN) are often intense sources of Lyman-continuum (LyC, or hydrogen ionising) photons resulting in the formation of regions of ionised gas in their surroundings (e.g. HII regions). The emission from these regions carries information about the physical conditions in the interstellar medium (ISM) as well as the source of the ionising photons themselves. Key properties that can be constrained include the star formation rate (e.g. Kennicutt & Evans 2012), gas metallicity (e.g. Tremonti et al. 2004), temperature, density, dust content (e.g. Reddy et al. 2015), and the presence of an AGN (e.g. Baldwin et al. 1981). Nebular line emission enables the accurate measurement of redshifts, and thus distances once a cosmological model is assumed.

While there has been extensive progress in observing line emission at low (e.g. Brinchmann et al. 2004) and intermediate (e.g. Steidel et al. 1996; Shapley et al. 2003) redshifts there are few direct constraints at high-redshift. This is predominantly due to lack of sensitive near-IR spectrographs, particularly at $> 2\mu$m where the rest-frame optical lines lie at $z > 4$, and the comparative lack of strong lines, other than Lyman-α, in the rest-frame UV. The small number of detections at high-redshift come overwhelmingly from Lyman-α (e.g. Stark et al. 2010; Pentericci et al. 2011; Stark et al. 2011; Caruana et al. 2012; Stark et al. 2013; Finkelstein et al. 2013; Caruana et al. 2014; Stark et al. 2017) though there has now been a handful of detections of the [CIV]λ1548 and [CIII],CIII]λ1907, 1090 lines (Stark et al. 2015a,b, 2017). The presence of extremely strong optical lines can also be indirectly inferred from their impact on broadband photometry (e.g. Schaerer & de Barros 2010; Stark et al. 2013; Wilkins et al. 2013; Smit et al. 2014; Wilkins et al. 2016a; De Barros et al. 2019) yielding constraints now available up to $z \approx 8$ (De Barros et al. 2019).

⋆ E-mail: s.wilkins@sussex.ac.uk

While existing observational constraints in the EoR are limited this will soon change with the arrival of the *Webb Telescope*. *Webb*'s NIRSpec instrument will provide deep near-IR single slit, multi-object, and integral field spectroscopy from $\sim 0.7-5\mu$m, while the NIRISS and NIRCam instruments will, together, provide wide field slitless spectroscopy over a similar range. This is sufficient to encompass all the strong optical lines to $z \sim 7$ with [OII] potentially accessible to $z \sim 12$. *Webb*'s mid-infrared instrument (MIRI) will provide mid-IR single slit, and slitless spectroscopy at $\lambda > 5\mu$m, albeit at much lower sensitivity and thus will likely only detect line emission for the brightest sources in the EoR.

The existing direct and indirect constraints and the nearing prospect of *Webb* motivates us to produce predictions for the nebular emission line properties of galaxies in the EoR. In this paper, we combine the large BlueTides hydrodynamical simulation with photoionisation modelling to predict the nebular line properties of galaxies in the EoR, specifically ($z = 8 \rightarrow 13$). As part of this paper we also explore some of the photon-ionisation modelling assumptions including the choice of stellar population synthesis (SPS) model and initial mass function (IMF). These predictions can be used to optimise the design of *Webb* surveys prior to launch, targeting emission lines in the EoR. The observation of these lines will also provide a powerful constraint on the physics incorporated into galaxy formation models.

This paper is structured as follows: in Section 2 we describe the BlueTides simulation and our methodology for calculating the nebular emission line properties. In Section 3 we present our predictions, including examining the effect of the choice of initial mass function and stellar population synthesis model (§3.3) and providing a comparison with existing observational constraints (§3.4). In Section 4 we present our conclusions. In Appendix A we briefly present an overview of the production of ionising photons by stellar populations and photoionisation modelling.

By default we make the following modelling choices: we assume the BPASS v2.2.1 SPS model (Stanway & Eldridge 2018; Eldridge et al. 2017)[1] and a modified version of the Salpeter IMF containing a flattened ($\alpha = -1.3$) power-law at low-masses ($m < 0.5\,M_\odot$). This IMF produces very similar (< 0.05 dex) results to the assumption of a Chabrier (2003) IMF but permits a fairer comparison with the alternative IMFs available for BPASS.

2 MODELLING NEBULAR EMISSION IN BLUETIDES

2.1 The BlueTides Simulation

The BlueTides simulation[2] (see Feng et al. 2015, 2016, for description of the simulation physics) is an extremely large cosmological hydrodynamical simulation designed to study the early phase of galaxy formation and evolution with a specific focus on the formation of the massive galaxies. BlueTides phase 1 evolved a $(400/h \approx 577)^3\,\mathrm{cMpc}^3$ cube to $z = 8$ using 2×7040^3 particles assuming the cosmological parameters from the *Wilkinson Microwave Anisotropy Probe* ninth year data release (Hinshaw et al. 2013). The properties of galaxies in the simulation are extensively described in Feng et al. (2015, 2016); Wilkins et al. (2016b,a); Waters et al. (2016a,b); Di Matteo et al. (2016); Wilkins et al. (2017, 2018). In this work we focus on galaxies with stellar masses $> 10^8\,M_\odot$ which contain at least approximately 100 star particles. Considering smaller galaxies runs the risk that the star formation history is not sufficiently sampled at young ages (see §2.2.1). While BlueTides contains supermassive black holes and even AGN dominated sources at $z = 8$ in this work we focus on the line emission arising solely from gas excited by stellar sources.

2.1.1 *Ages and Metallicities of Galaxies in BLUETIDES*

As emission line luminosities and equivalent widths are predominantly driven by galaxy star formation and metal enrichment histories it is useful to explore the average ages and metallicities predicted by BlueTides. The mean stellar age and mean metallicity of young ($< 10\,\mathrm{Myr}$) stars are shown as a function of stellar mass for a range of redshifts in Figure 1. These correlations were previously discussed in more detail in Wilkins et al. (2017) while a more detailed analysis of the joint star formation and metal enrichment history is presented in Fairhurst et al. *in-prep*. In short, the mean stellar age appears to show little dependence on mass but evolves strongly with redshift while the mean metallicity of young stars shows a power-law dependence ($Z \propto M^{0.4}$) on stellar mass but little evolution with redshift.

2.2 Nebular Emission Modelling

To model the nebular emission from entire galaxies we start by associating each star particle with an intrinsic stellar spectral energy distribution (SED) based on its age and metallicity. Using this SED we then calculate the corresponding nebular emission using the 2017 (C17.01) version of the popular CLOUDY code (Ferland et al. 2017)[3]. The resulting *intrinsic* nebular emission associated with each galaxy is then simply the sum over all star particles. Additional details on our photoionisation modelling methodology are given in Appendix A.

2.2.1 *Star Formation History Sampling Effects*

The Lyman continuum photon production rate is a strong function of the age, and to a lesser extent, metallicity of the stellar population (see §A1). As the star formation history of each galaxy is sampled, at the lowest masses considered, by a small (~ 100) number of individual star particles, this raises the possibility that the predicted line properties differs from the truth because of SFH sampling affects. To explore the potential extent of this effect we re-sample the average star formation history of galaxies at $z = 8$ using different numbers of fixed mass particles ($n = 10^2 - 10^4$); corresponding roughly to stellar masses of $10^8 - 10^{10}\,M_\odot$. The result of this analysis is shown in Fig. 2. This test reveals that there is no

[1] https://bpass.auckland.ac.nz
[2] http://bluetides-project.org/
[3] https://www.nublado.org

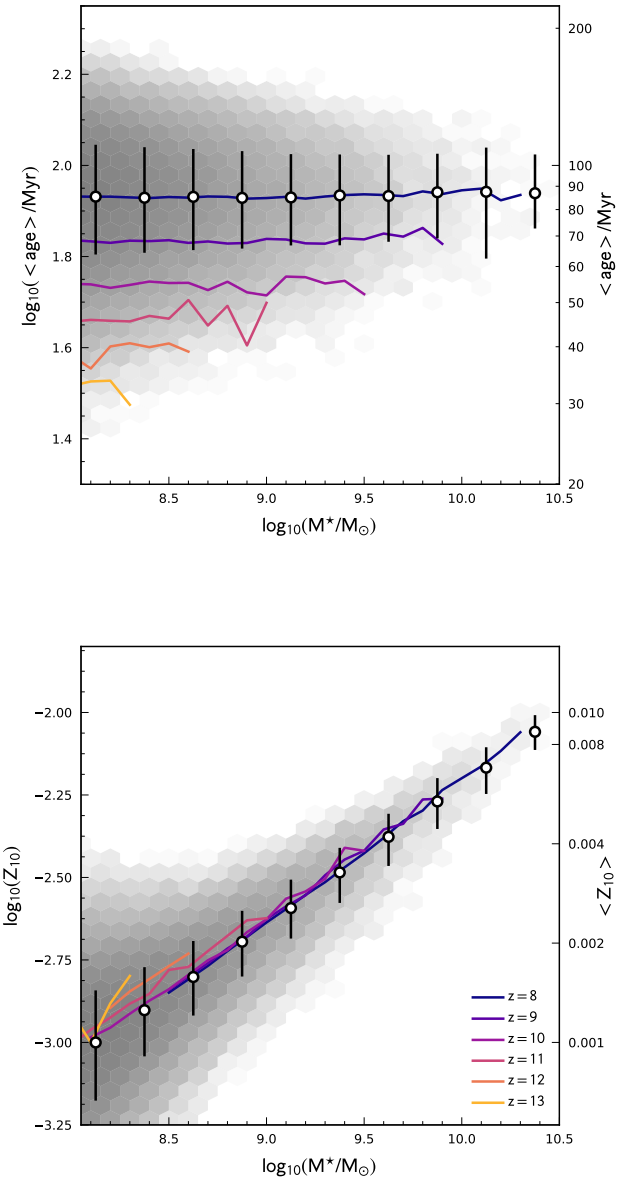

Figure 1. The mass-weighted average age (top) and average metallicity of star particles with ages $< 10\,\mathrm{Myr}$ (bottom) as a function of stellar mass for $z \in \{8, 9, 10, 11, 12, 13\}$. The solid lines show the median age/metallicity in 0.1 dex wide $\log_{10}(M_\star/\mathrm{M}_\odot)$ bins. The 2D histogram shows the distribution of stellar masses and mean ages/metallicities at $z = 8$ using a logarithmic scale.

significant bias in the average (median or mean) of the predicted line luminosity (in this case Hα), even at low-masses. However, at low-masses there is considerable scatter (≈ 0.1 dex for $n = 300$ particles / $M_\star \approx 2.5 \times 10^8\,\mathrm{M}_\odot$). This type of scatter could potentially flatten the predicted luminosity function at low-luminosities.

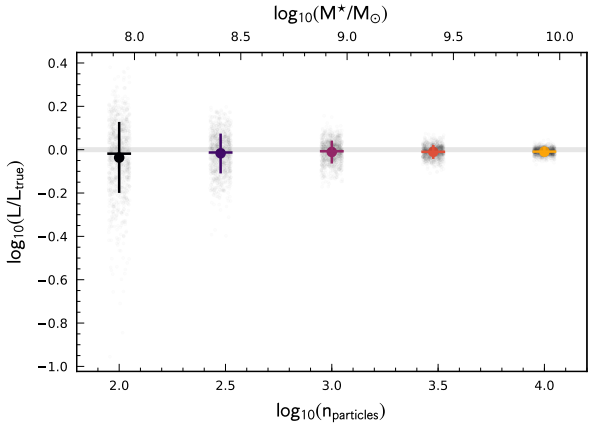

Figure 2. The ratio of the modelled line luminosity compared to the true luminosity as a function of the number of particles used to sample the star formation history. The top-axis shows the corresponding stellar mass assuming the mean BlueTides stellar particle mass.

2.3 Modelling attenuation by dust

Dust attenuation in BlueTides is modelled using a simple scheme which links the smoothed metal density integrated along lines of sight to each star particle within each galaxy to the dust optical depth in the V-band (550 nm). Attenuation at other wavelengths is determined using a simple attenuation curve of the of the form,

$$\tau_\lambda = \tau_V \times (\lambda/550\mathrm{nm})^{-1}. \quad (1)$$

This model has a single free parameter which effectively links the surface density of metals to the optical depth. This parameter is tuned to recover the shape of the of the observed $z = 8$ far-UV luminosity function. For a full description see Wilkins et al. (2017).

This simple model for the reprocessing of light by gas and dust effectively assumes that ionising photons produced by star particles are reprocessed by the gas before being absorbed by dust. For a given star particle this means the stellar and nebular emission are equally affected by dust, leaving line equivalent widths unaffected[4]. In reality it is likely that at least some fraction of ionising photons are absorbed by dust prior to being reprocessed.

3 PREDICTIONS FOR BLUETIDES

Using the methodology outlined above we calculate the luminosities and equivalent widths of twelve lines for all galaxies in BlueTides at $z = 8 - 13$ with $M_\star > 10^8\,\mathrm{M}_\odot$. The observed wavelength of the twelve lines along with the ranges probed by various *Webb* instruments are shown in Fig. 3.

[4] While true for a single star particle, this is not necessarily true for an entire galaxy. For example, if star particles associated with strong nebular emission are more heavily attenuated than others the equivalent width of a line can be suppressed.

[!h]

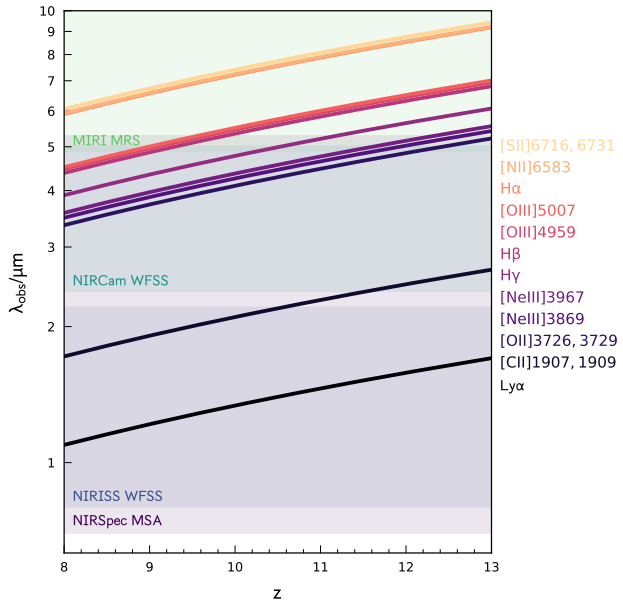

Figure 3. The observed wavelength of the twelve lines considered in this work along with the ranges probed by various *Webb* instruments.

3.1 Line Luminosities and Equivalent Width Distributions

Predictions for the line luminosities and EWs and their dependence with stellar mass and UV luminosity are summarised, for 6 prominent lines, in Fig. 4. These predictions assume the BPASS v2.2.1 SPS model and a modified Salpeter IMF. In Appendix B we also provide more detailed plots for each individual line or doublet. Tabulated results for all twelve lines are also all available in electronic form here.

In summary, the luminosity function of each line broadly follows a similar trend to the UV luminosity function: intrinsically the LF is approximated by a single power-law; the inclusion of dust however causes a strong break at high luminosities. Like the UV LF the line luminosity function evolves strongly with redshift, increasing by a factor ≈ 1000 from $z = 13 \rightarrow 8$.

Line EWs all increase to higher redshift, however their dependence on stellar mass is more complex due to the correlation of stellar mass with metallicity (§2.1.1) and the sensitivity of individual line luminosities to the metallicity (§A2.1). For example the EW of the hydrogen recombination lines drops at higher stellar mass while that of the [OII]3726, 3729 line peaks at $M^\star \sim 10^{9.5}\,\mathrm{M}_\odot$ (at $z = 8$).

3.2 Line Emission as a Tracer of Star Formation

As the LyC photon production drops off dramatically at ages $> 10\,\mathrm{Myr}$, hydrogen recombination line luminosities are often held as a gold standard of star formation activity tracers (Kennicutt & Evans 2012). In Fig. 5 we compare the intrinsic Hα luminosity to the recent ($\leq 10\,\mathrm{Myr}$) star formation activity as a function of stellar mass and redshift. At high-masses, where star formation history sampling effects (see §2.2.1) are negligible the scatter in the ratio is very small $\log_{10}[(L_{H\alpha}/\mathrm{SFR})/\mathrm{erg\,s^{-1}\,M_\odot^{-1}\,yr}] \approx 0.05$ confirming the tight relation between line luminosity and star formation activity. There is also a slight decline with increasing stellar mass attributable to an increase in the stellar metallicity (see Fig. 1) and thus the decline in the LyC photon production rate (see Fig. A1). The increase in the scatter at low stellar masses can be attributed to the sampling effects discussed in §2.2.1.

However, the calibration inferred from this analysis is significantly different (≈ 0.45 dex higher) from the value proposed by Kennicutt & Evans (2012). This reflects both the fact that the BPASS models produce more LyC photons and that the metallicity implicit in the Kennicutt & Evans (2012) calibration is higher than predicted by BLUETIDES.

3.3 The effect of the choice of IMF and SPS model

We also explore the effect of changing the choice of stellar population synthesis model and/or initial mass function on the luminosities and equivalent widths. However, these changes are only made at the post-processing stage and are thus not self-consistent. For example, self-consistently adopting an alternative IMF would significantly affect the production of metals which would also impact line ratios and luminosities (e.g. **?**). A summary of these changes, relative to our default choices, are shown in Fig. 6.

Unsurprisingly, increasing the fraction of high-mass stars, either by extending the high-mass cutoff or flattening the high-mass slope results in increased line luminosities and equivalent widths. As continuum luminosities are also increased the impact on equivalent widths is smaller than on line luminosities themselves. It is also important to note that flattening the IMF in this way would also increase the far-UV continuum luminosities of galaxies breaking the otherwise good agreement with observations (see Wilkins et al. 2017). This could however be ameliorated by having more aggressive dust attenuation. The effect of steepening the slope produces the opposite effect. Steepening the IMF to this extent will also significantly decrease the far-UV continuum luminosities again breaking the good agreement with observational constraints. In this case the good agreement can not be recovered without more drastic changes to the simulation physics.

Adopting previous releases (2.2 or 2.1) of the BPASS models produces only relatively small changes (< 0.1 dex) to the predicted line luminosities and equivalent widths. On the other hand adopting the PEGASE.2 SPS model (and $m_{\mathrm{up}} = 100\,\mathrm{M_{odot}}$) produces a significant decrease in the luminosities and equivalent widths relative to our default model. For most lines luminosities drop by ~ 0.5 dex while equivalent widths drop by ~ 0.3. While some of this decrease can be attributed to the small upper-mass cutoff of the IMF most of the effect is attributed to wider modelling differences between PEGASE.2 and BPASS, in particular the inclusion of binary stars in the latter.

[!h]

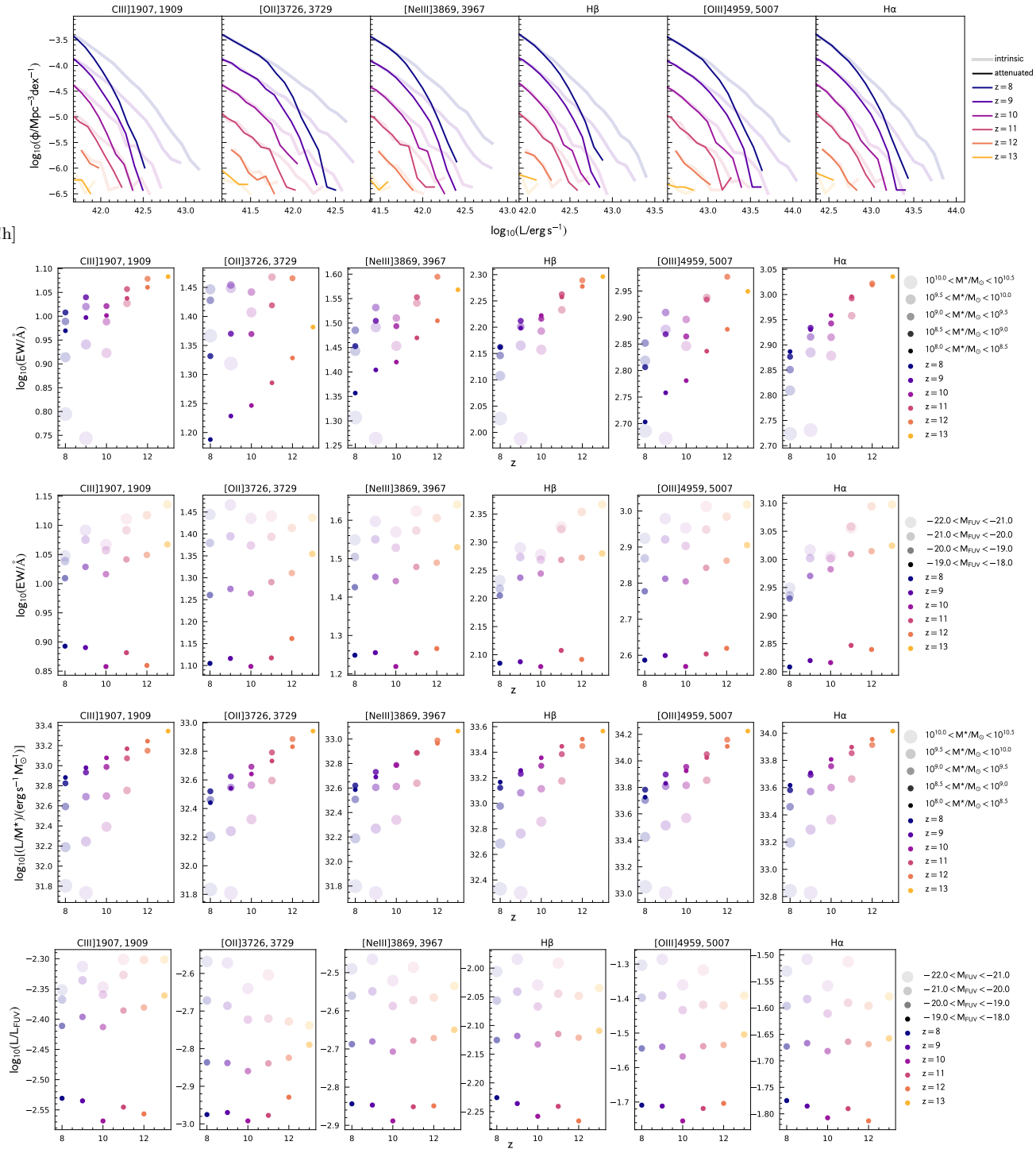

Figure 4. Predictions for the properties of 6 prominent UV and optical lines in BlueTides. In the top panel we show both the intrinsic and dust-attenuated luminosity functions for each line at $z \in \{8, 9, 10, 11, 12, 13\}$. In the next two rows we show the median attenuated equivalent width in bins of stellar mass and UV luminosity respectively. In the fourth row we show the median specific line luminosity ($L/M_\star$) in stellar mass bins while in the final row we show the median ratio of the line luminosity to the UV luminosity in bins of UV luminosity.

3.4 Comparison with existing observational constraints

As noted in the introduction there remain few constraints (direct or otherwise) on line emission at very high-redshift. The majority of direct constraints come from observations of Lyman-α (e.g. Stark et al. 2010; Pentericci et al. 2011; Stark et al. 2011; Caruana et al. 2012; Stark et al. 2013; Finkelstein et al. 2013; Caruana et al. 2014; Stark et al. 2017). However, the Lyman-α line is resonantly scat-

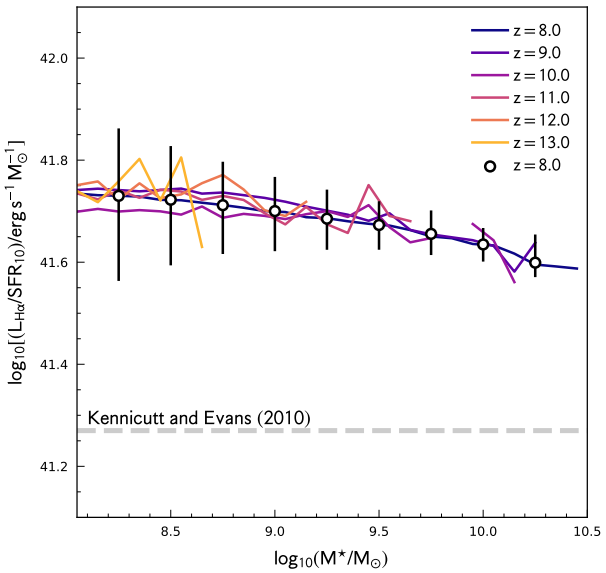

Figure 5. The ratio of the intrinsic Hα line luminosity to the recent star formation activity (the total mass in stars formed in the last 10 Myr) as a function of stellar mass. The horizontal line denotes the value suggested by Kennicutt & Evans (2012).

tered by the ISM/IGM significantly complicating its modelling (see Smith et al. 2019). For this reason we have omitted a detailed comparison with Lyman-α observations. We do however nevertheless make predictions for the intrinsic Lyman-α properties, where intrinsic in this context includes dust attenuation but not scattering by the ISM/IGM. These predictions are presented in Appendix B.

Recently Stark et al. (2015a) and Stark et al. (2017) have obtained constraints on the [CIII],CIII] doublet at $z = 6-8$. These constraints are shown in Fig. 7 alongside predictions from BlueTides. These constraints are broadly in line with BlueTides predictions with the exception of EGS-z8-1 (Stark et al. 2017) which has a measured EW ~ 0.3 dex above the predictions. However, it is important to note that our predictions do not include an AGN component which may explain the high EW observed in EGS-z8-1 (Nakajima et al. 2018).

Indirect constraints on the strength of the strongest optical lines are possible through the effect of these lines on broad-band photometry (e.g. Schaerer & de Barros 2010; Stark et al. 2013; Wilkins et al. 2013; Smit et al. 2014; Wilkins et al. 2016a; De Barros et al. 2019). De Barros et al. (2019) recently combined *Hubble* and *Spitzer* observations probing the rest-frame UV and optical to constrain the prominent Hβ and [OIII]λ4959,5007 lines at $z \approx 8$. As shown in Fig. 8 the Hβ + [OIII] EW distribution measured by De Barros et al. (2019) closely overlaps with that predicted by BlueTides.

Unfortunately this good agreement is not seen in the luminosity function, as shown in Fig. 9, which is systematically offset to higher luminosities (~ 0.3 dex) or higher space densities (~ 0.7 dex). The cause of this discrepancy appears to lie in the relation between the combined line luminosity and the far-UV luminosity, which is used to convert the observed far-UV luminosity function to a line luminosity function. The individual values measured by De Barros et al. (2019) for this are shown in Fig. 10 and are compared to the values predicted by BlueTides. The measured values appear to be on average ~ 0.3 dex higher than predicted by BlueTides. As many of the measured values are above the intrinsic expectation (see Fig. 11) one interpretation of this discrepancy is that De Barros et al. (2019) measure higher dust attenuations than predicted by BlueTides. It is also possible that differences between the measured and predicted values of the metallicity, age, ionisation parameter, and hydrogen density can have an effect. Given the limited observational constraints such differences may not be surprising considering the range of degeneracies present.

With the arrival of the *Webb Telescope* it will be possible to obtain direct measurements of individual line luminosities and equivalent widths for a large range of galaxies at $z \sim 8$ and beyond providing a much clearer assessment of whether these predictions match the real Universe.

4 CONCLUSIONS

Using the large cosmological hydrodynamical simulation BlueTides combined with photoionisation modelling we have made detailed predictions for the luminosities (including luminosity function) and equivalent widths of twelve prominent rest-frame UV and optical emission lines for galaxies with $M^\star > 10^8\,M_\odot$ across the EoR ($8 < z < 13$).

- The predicted strength of line luminosities and equivalent widths is sensitive to a range of modelling assumptions and in particular the choice of stellar population synthesis model and initial mass function.
- While the Hα luminosity is found to be strongly correlated with recent star formation activity we find a large offset ($0.3 - 0.4$ dex higher) between the popular Kennicutt & Evans (2012) calibration and our results. This reflects both the adoption of the BPASS stellar population synthesis models and the lower metallicity of the stellar populations.
- At present there are few observational constraints on line emission available in the EoR with only a handful of direct constraints on the [CIII],CIII] doublet along with indirect constraints on Hβ and [OIII]λ4959,5007 based on *Spitzer* photometry. Our predictions match indirect constraints on the Hβ + [OIII]λ4959,5007 equivalent width distribution but fail to match the inferred luminosity function.

Acknowledgements

We acknowledge support from NSF ACI-1036211, NSF AST-1009781, and NASA ATP grants NNX17AK56G and 80NSSC18K1015. The BlueTides simulation was run on facilities at the National Center for Supercomputing Applications. TDM acknowledges support from Shimmins and Lyle Fellowships at the University of Melbourne.

REFERENCES

Baldwin J. A., Phillips M. M., Terlevich R., 1981, Publications of the Astronomical Society of the Pacific, 93, 5

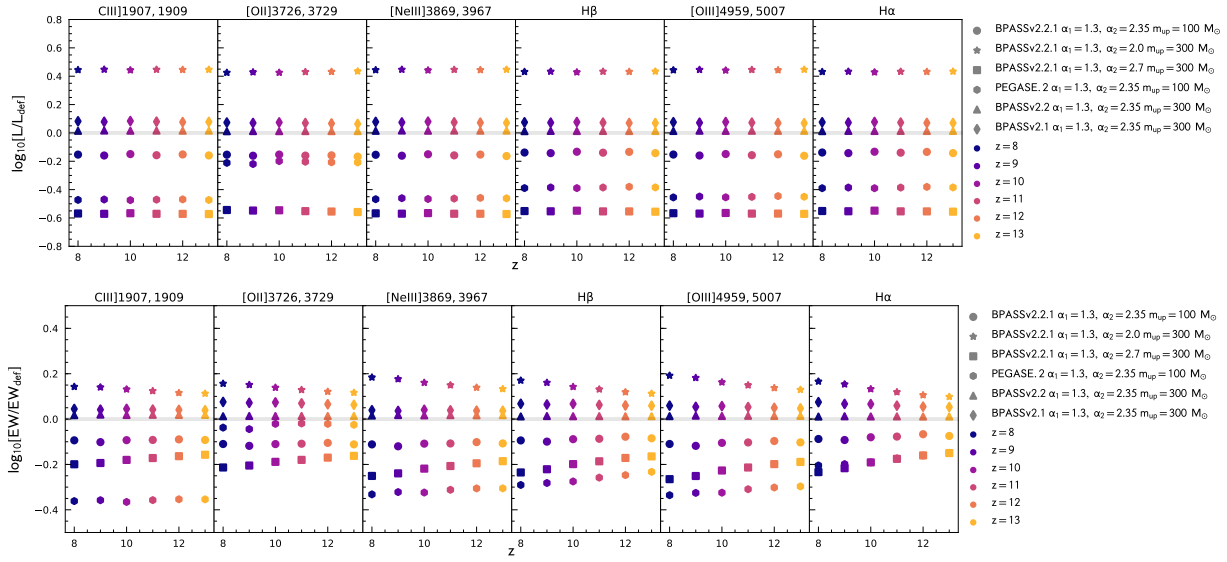

Figure 6. The effect of changing the choice of stellar population synthesis model and/or initial mass function on the luminosities and equivalent widths of the 6 lines relative to our default choices (BPASSv2.2.1, $\alpha_2 = 2.35$, $m_{\rm up} = 300\,{\rm M}_\odot$).

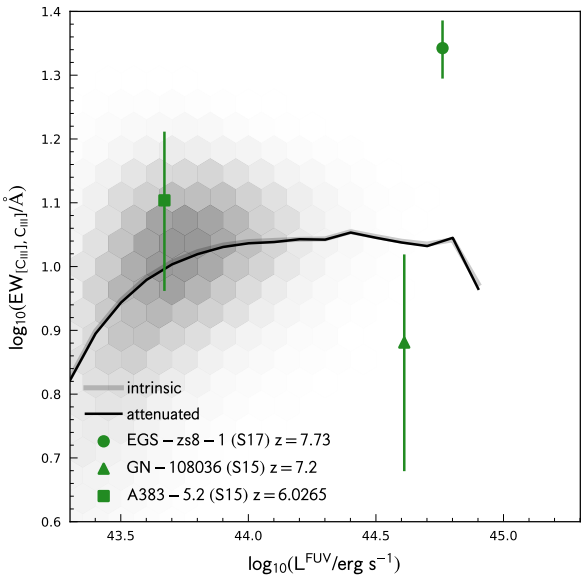

Figure 7. The predicted distribution of [CIII],CIII] equivalent width and observed far-UV luminosity at $z \sim 8$. Points denote individual objects from $z = 5 - 8$.

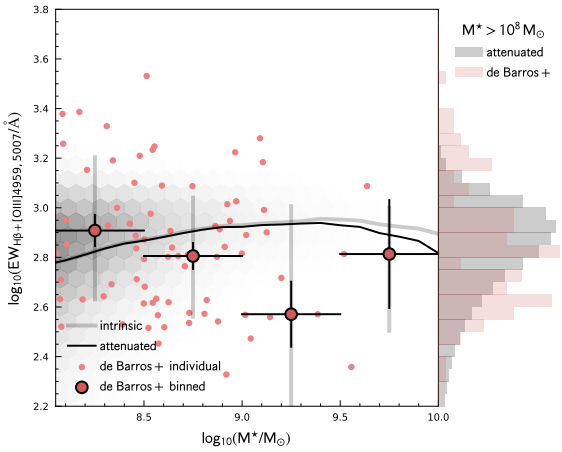

Figure 8. The observed De Barros et al. (2019) and predicted distribution of combined Hβ and [OIII]λ4959,5007 equivalent widths and stellar masses at $z \sim 8$. The small red circles show the individual measurements from De Barros et al. (2019) while the large point denote the median value in 0.5 dex wide bins of stellar mass. The small and large error bars denote the error on the median and the 16-84th percentile range respectively. The dark and light solid lines show the intrinsic and attenuated predictions from BlueTides respectively. The histograms on the right hand side show the distribution of equivalent widths for galaxies with $M^\star > 10^8\,{\rm M}_\odot$.

Brinchmann J., Charlot S., White S. D. M., Tremonti C., Kauffmann G., Heckman T., Brinkmann J., 2004, MNRAS, 351, 1151
Caruana J., Bunker A. J., Wilkins S. M., Stanway E. R., Lacy M., Jarvis M. J., Lorenzoni S., Hickey S., 2012, MNRAS, 427, 3055
Caruana J., Bunker A. J., Wilkins S. M., Stanway E. R., Lorenzoni S., Jarvis M. J., Ebert H., 2014, MNRAS, 443, 2831
Chabrier G., 2003, PASP, 115, 763
Charlot S., Longhetti M., 2001, MNRAS, 323, 887
De Barros S., Oesch P. A., Labbé I., Stefanon M., González V., Smit R., Bouwens R. J., Illingworth G. D., 2019, arXiv e-prints, p. arXiv:1903.09649
Di Matteo T., Croft R. A. C., Feng Y., Waters D., Wilkins S., 2016, preprint, (arXiv:1606.08871)
Eldridge J. J., Stanway E. R., Xiao L., McClelland L. A. S., Taylor G., Ng M., Greis S. M. L., Bray J. C., 2017, Publications of the Astronomical Society of Australia, 34, e058
Feltre A., Charlot S., Gutkin J., 2016, MNRAS, 456, 3354

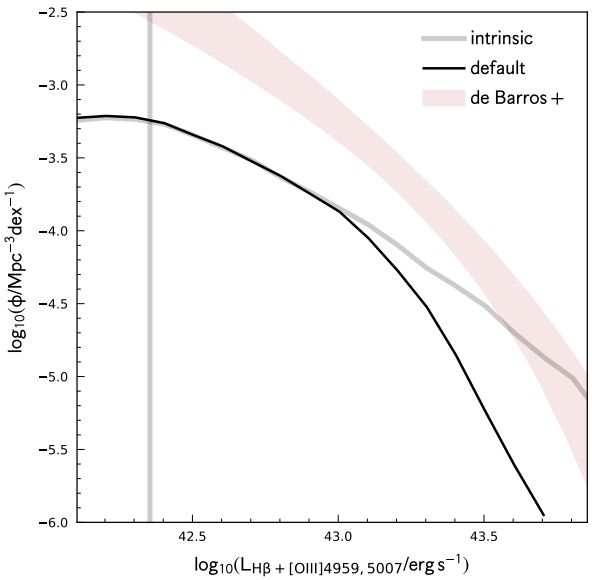

Figure 9. The observed De Barros et al. (2019) and predicted combined Hβ and [OIII]λ4959,5007 line luminosity function at $z \sim 8$. The vertical line denotes the approximate completeness limit of the predicted line luminosity function.

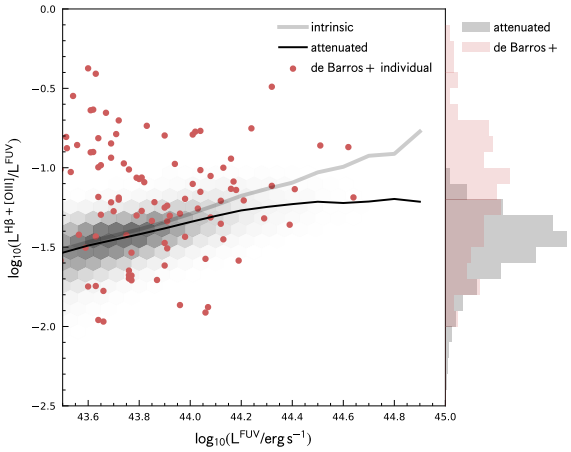

Figure 10. The observed De Barros et al. (2019) and predicted distribution of the ratio of the Hβ and [OIII]λ4959,5007 line luminosities to the far-UV luminosity and far-UV luminosities at $z \sim 8$. The small red circles show the individual measurements from De Barros et al. (2019). The dark and light solid lines show the intrinsic and attenuated predictions from BlueTides respectively. The histograms on the right hand side show the distribution of ratios for galaxies with $M^\star > 10^8$ M$_\odot$.

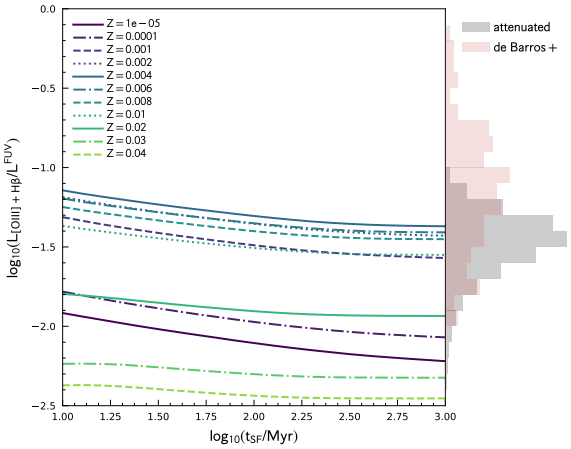

Figure 11. The Hβ and [OIII]λ4959,5007 line luminosities - far-UV luminosity ratio measured by De Barros et al. (2019) compared to predictions from photoionisation modelling assuming a constant star formation activity ($t = 10 \rightarrow 1000$ Myr) and a range of metallicities. The histograms on the right hand side show both the observed and predicted distribution of ratios for galaxies with $M^\star > 10^8$ M$_\odot$.

Feng Y., Di Matteo T., Croft R., Tenneti A., Bird S., Battaglia N., Wilkins S., 2015, ApJ, 808, L17
Feng Y., Di-Matteo T., Croft R. A., Bird S., Battaglia N., Wilkins S., 2016, MNRAS, 455, 2778
Ferland G. J., et al., 2017, Rev. Mex. Astron. Astrofis., 53, 385
Finkelstein S. L., et al., 2013, Nature, 502, 524
Fioc M., Rocca-Volmerange B., 1997, A&A, 326, 950
Gutkin J., Charlot S., Bruzual G., 2016, MNRAS, 462, 1757
Hinshaw G., et al., 2013, ApJS, 208, 19
Kennicutt R. C., Evans N. J., 2012, ARA&A, 50, 531
Nakajima K., et al., 2018, A&A, 612, A94
Pentericci L., et al., 2011, ApJ, 743, 132
Reddy N. A., et al., 2015, ApJ, 806, 259
Schaerer D., de Barros S., 2010, A&A, 515, A73
Shapley A. E., Steidel C. C., Pettini M., Adelberger K. L., 2003, ApJ, 588, 65
Smit R., et al., 2014, ApJ, 784, 58
Smith A., Ma X., Bromm V., Finkelstein S. L., Hopkins P. F., Faucher-Giguère C.-A., Kereš D., 2019, MNRAS, 484, 39
Stanway E. R., Eldridge J. J., 2018, MNRAS, 479, 75
Stark D. P., Ellis R. S., Chiu K., Ouchi M., Bunker A., 2010, MNRAS, 408, 1628
Stark D. P., Ellis R. S., Ouchi M., 2011, ApJ, 728, L2
Stark D. P., Schenker M. A., Ellis R., Robertson B., McLure R., Dunlop J., 2013, ApJ, 763, 129
Stark D. P., et al., 2015a, MNRAS, 450, 1846
Stark D. P., et al., 2015b, MNRAS, 454, 1393
Stark D. P., et al., 2017, MNRAS, 464, 469
Steidel C. C., Giavalisco M., Pettini M., Dickinson M., Adelberger K. L., 1996, ApJ, 462, L17
Tremonti C. A., et al., 2004, ApJ, 613, 898
Waters D., Di Matteo T., Feng Y., Wilkins S. M., Croft R. A. C., 2016b, preprint, (arXiv:1605.05670)
Waters D., Wilkins S., Di Matteo T., Feng Y., Croft R., Nagai D., 2016a, preprint, (arXiv:1604.00413)
Wilkins S. M., et al., 2013, MNRAS, 435, 2885
Wilkins S. M., Feng Y., Di-Matteo T., Croft R., Stanway E. R., Bunker A., Waters D., Lovell C., 2016a, preprint, (arXiv:1605.05044)
Wilkins S. M., Feng Y., Di-Matteo T., Croft R., Stanway E. R., Bouwens R. J., Thomas P., 2016b, MNRAS, 458, L6
Wilkins S. M., Feng Y., Di-Matteo T., Croft R., Lovell C. C., Waters D., 2017, preprint, (arXiv:1704.00954)
Wilkins S. M., Feng Y., Di Matteo T., Croft R., Lovell C. C.,

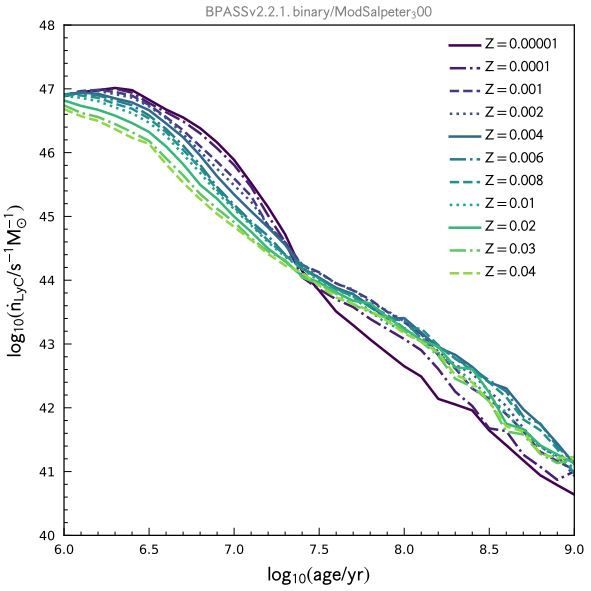

Figure A1. The production rate of Lyman continuum (LyC) photons (HI ionising) produced by a simple stellar population (SSP) per unit initial mass as a function of age for a range of different metallicities.

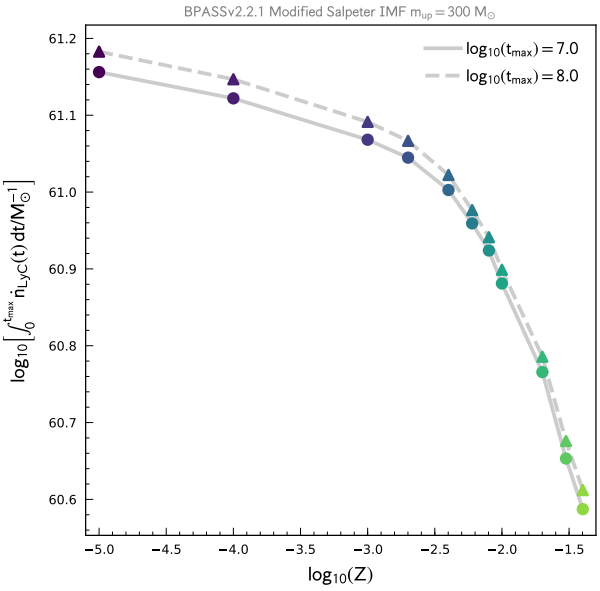

Figure A2. The total number of LyC photons produced by SSP over the first 10 and 100 Myr as a function of metallicity.

Thomas P., 2018, MNRAS, 473, 5363

APPENDIX A: PHOTOIONISATION MODELLING

To predict the emission line properties of galaxies in the BLUETIDES simulation we assume that each star particle forms its own HII region based on its age and metallicity.

Because each star particle is modelled as a simple (with a single age and metallicity) stellar population (SSP) it is useful to (in §A1) explore how the rate of Lyman continuum (LyC) photon production, and the hardness of the ionising photon continuum, is affected by the age, metallicity, initial mass function (IMF), and choice of stellar population synthesis (SPS) model. In §A2 we then describe our photoionisation modelling procedure and explore how various lines are sensitive to parameters such as the gas/stellar metallicity, ionisation parameter, and hydrogen density.

A1 The Production of Ionising Photons

The LyC production rate of a SSP depends on both its age and metallicity. This is demonstrated in Fig. A1, where we show the LyC production rate $\dot{n}_{\rm LyC}$ as a function of age for a range of different metallicities assuming the BPASS model and a modified Salpeter IMF extending to 300 $M_\odot$. The production rate drops rapidly after the first few million years at higher ages and metallicities, declining by $\sim 10-100$ as the population ages from 1 $\rightarrow$ 10 Myr and then again by a factor of ~ 100 from $t = 10 \rightarrow 100$ Myr. At young ages (< 20 Myr) the lowest metallicity populations can produce up-to 10 times as many LyC photons, though at later times this trend reverses.

The overall difference in the production of LyC photons as a function of metallicity is summarised in Fig. A2 where we show the *total* number of LyC photons produced by an SSP from $t = 0 \rightarrow 10^7$ yr and $t = 0 \rightarrow 10^8$ yr. The lowest metallicity modelled ($Z = 10^{-5}$) SSP considered produces approximately double the number LyC photons over its lifetime compared to $Z = 0.01$.

A1.1 The Ionising Photon Hardness

More complex atoms have a range of potential ionisation states each excited by photons of different energies. For example, Helium can be singly ionised by photons with $E_\gamma > 24.6$ eV and doubly ionised by those with $E_\gamma > 54.4$ eV. For this reason it is useful to also consider the ionising photon hardness, essentially a ratio of the number of more energetic photons to $\dot{n}_{\rm LyC}$. The left panel of Fig. A3 shows the hardness the LyC by comparing the number of LyC and OII (> 35.1 eV) energy photons as a function of age for two metallicities $Z \in \{0.02, 0.004\}$. At the youngest ages the higher metallicity SSP produces significantly fewer (~ 1 dex) harder photons. For older (> 10 Myr) populations the hardness is similar.

A1.2 The Choice of Initial Mass Function and SPS Model

It is crucial to note that both the number of LyC photons and the shape of the ionising spectrum predicted for a given SSP is sensitive to the a range of stellar evolution and atmosphere modelling assumptions and thus choice of stellar population synthesis (SPS) model (see also **??**). The middle panel of Fig. A3 shows a comparison between $\dot{n}_{\rm LyC}$ for different SPS models/versions; these include the three most re-

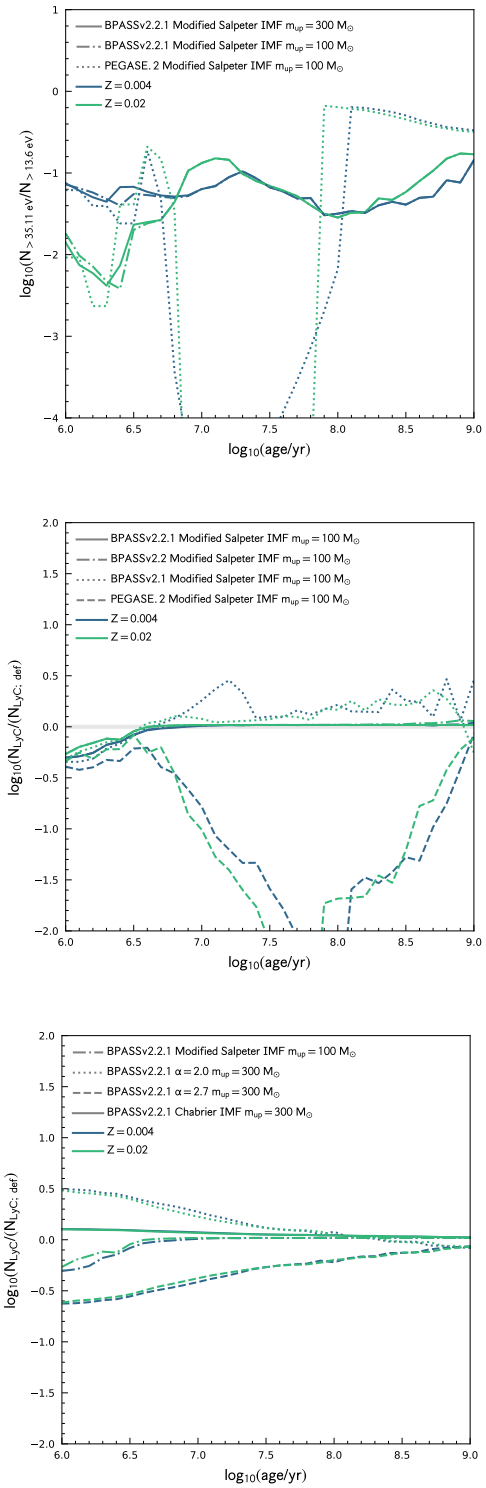

Figure A3. *Left:* The hardness of the ionising of photon spectrum (defined as the ratio of to HI ionising photons) as a function of age for two metallicities and three SPS model / IMF combinations. *Centre:* The difference between the number of LyC photons produced assuming alternative SPS models. *Right:* The difference between the number of LyC photons produced assuming alternative initial mass functions.

cent versions of BPASS (v2.2.1, v2.2, v2.1) and the PEGASE.2 model (Fioc & Rocca-Volmerange 1997). This analysis reveals relatively small differences between the different BPASS versions but larger differences between BPASS and PEGASE.2. This difference is particularly acute at ages > 5 Myr where the LyC production rate predicted by PEGASE.2 drops of much more rapidly than in BPASS. The left panel of Fig. A3 shows the difference in the hardness between the default model and BPASS; again, the most notable feature is the difference at > 5 Myr.

Both the production rate and hardness are also affected by the choice of initial mass function (IMF). The right hand panel of Fig. A3 shows the production rate relative to our default model for several different high-mass slopes $\alpha \in \{2.0, 2.35, 2.7\}$ and for a lower ($100\,\mathrm{M}_\odot$) high-mass cut-off. Assuming a shallower slope ($\alpha = 2.0$) yields more around double the number of LyC photons overall with the enhancement decreasing with age. Assuming a steeper slope has the opposite effect albeit with a slightly larger magnitude. Adopting a lower high-mass cut-off reduces the number of LyC photons produced at the youngest ages, overall leading to around $\sim 30 - 50\%$ less LyC photons produced by the SSP over its lifetime, depending on the metallicity.

A2 Photoionisation Modelling

We now turn our attention to modelling the nebular continuum and line emission associated with a SSP. To do so we take advantage of the 2017 (C17.01) version of the popular CLOUDY code (Ferland et al. 2017)[5].

To model the nebular emission associated with a stellar population we adopt a similar approach to Charlot & Longhetti (2001) (see also Gutkin et al. 2016; Feltre et al. 2016). Like these works we choose characterise our photoionisation modelling using the density of hydrogen (n_H) and ionisation parameter at the Stromgren radius U_S. This is defined as,

$$U_S \propto \left(Q\epsilon^2 n_H\right)^{1/3} \tag{A1}$$

where ϵ is the effective gas filling factor.

We differ from previous approaches by parameterising models for the ionising spectrum in terms of an ionisation parameter defined at a reference age ($t = 1\,\mathrm{Myr}$) and metallicity ($Z = 0.02$) - $U_{S,\mathrm{ref}}$. Because of this the actual ionisation parameter passed to CLOUDY depends on the ionising photon production rate relative to the reference value, i.e.

$$U_S = U_{S,\mathrm{ref}} \left(\frac{Q}{Q_{\mathrm{ref}}}\right)^{1/3}. \tag{A2}$$

This ensures that the assumed geometry of the HII region, encoded in the $\epsilon^2 n_H$ term, is fixed for different metallicities/ages. By default we assume $\log_{10}(U_{S,\mathrm{ref}}) = -2$ and $\log_{10}(n_H/\mathrm{cm}^{-3}) = 2.5$.

We further assume that the metallicity of the HII region is the same as the stellar population and adopt the same interstellar abundances and dust depletion factors as Gutkin et al. (2016). It is however worth noting that the detailed elemental abundances assumed as a function of metallicity

[5] https://www.nublado.org

differ between that assumed in stellar population synthesis models and what we assume for the ISM.

A2.1 Line Luminosities and Equivalent Widths

Using the modelling procedure described above we now make predictions for line luminosity and equivalent widths. We concentrate here on 12 prominent UV and optical lines. In making these predictions we assume a constant star formation history with fixed metallicity.

Fig. A4 shows the predicted line luminosities (per unit stellar mass) and equivalent widths (EWs) for a range of prominent rest-frame UV and optical emission lines as a function of metallicity. In both cases we assume continuous star formation for 10 Myr. The luminosity of the hydrogen lines largely track the change in the LyC production rate with metallicity with the luminosity dropping by ~ 0.5 dex over the metallicity range considered. The non-hydrogen lines exhibit more complicated behaviour with an increase to $Z \sim 10^{-2.5}$ before declining to higher metallicities. The rapid increase broadly reflects the increasing abundance of each element in the ISM while the drop at high metallicities reflects the decline in the number of suitably energetic photons. The metallicity dependence of the EW of each line exhibits a similar behaviour, albeit often with reduced magnitude.

The equivalent width of any line is also sensitive the star formation history of the stellar population. Fig. A5 shows how the equivalent width of Hα varies with the duration of continuous star formation for a range of metallicities. The equivalent width declines from $\sim 1000 - 2000$ after to 10 Myr to $\sim 150 - 300$ after 1 Gyr.

A2.2 The Effect of Photoionisation Modelling Assumptions

The luminosity and EW width of each line is also sensitive to additional modelling assumptions including the choice of SPS model, IMF, but also the parameters encapsulating the geometry, density, and excitation of the H II region. As noted above we parameterise these in terms of the ionisation parameter, which effectively encodes the geometry of the region, and the hydrogen density.

Fig. A6 demonstrates the effect on changing both the reference ionisation parameter $U_{S,\mathrm{ref}}$ and hydrogen density n_H on the strengths of the same 12 prominent lines considered previously.

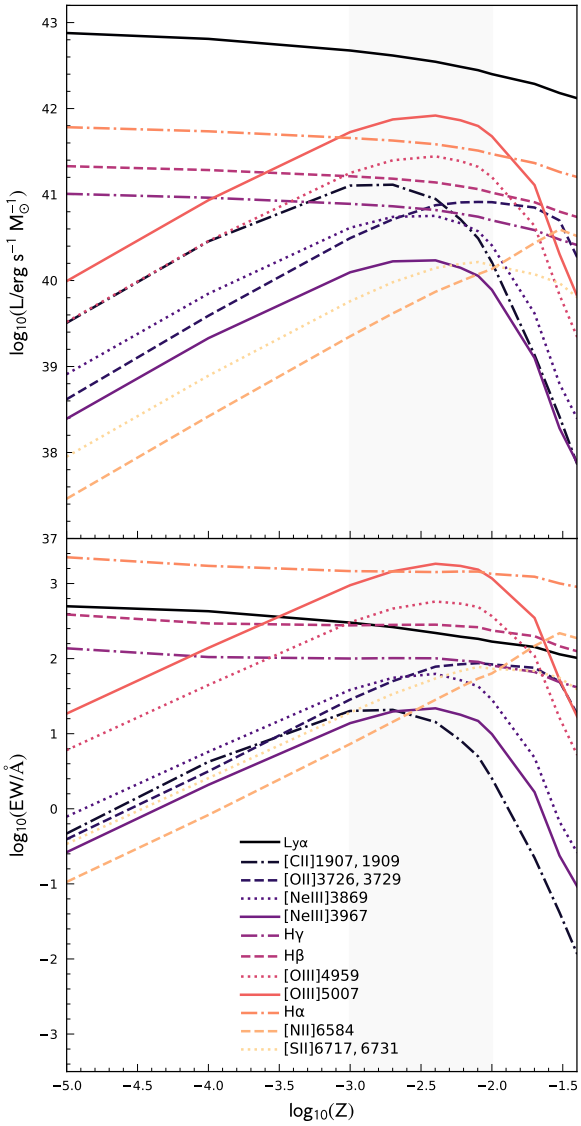

Figure A4. The predicted intrinsic luminosity (top) and equivalent width (bottom) as a function of metallicity for a range of prominent emission lines in the rest-frame UV and optical. In both cases we assume constant star formation for 10 Myr. The thick grey band denotes the rough range of metallicities predicted by BlueTides for galaxies with $M^* > 10^8\,\mathrm{M}_\odot$.

APPENDIX B: DETAILED PREDICTIONS FOR INDIVIDUAL LINES

In Figs. B1-B4 we show the EW and luminosity as a function of stellar mass and observed UV luminosity for each line in addition to the luminosity function. Tabulated values for each line and redshift are available at `https://github.com/stephenmwilkins/BluetidesEmissionLines_Public`.

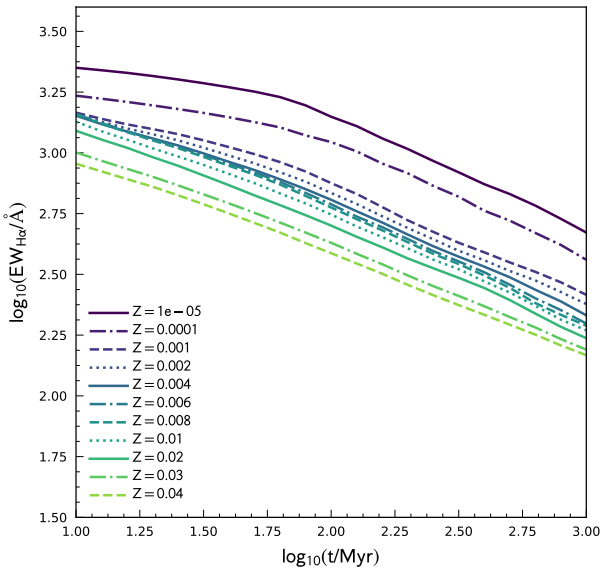

Figure A5. The evolution of the Hα equivalent width assuming continuous star formation for a range of metallicities.

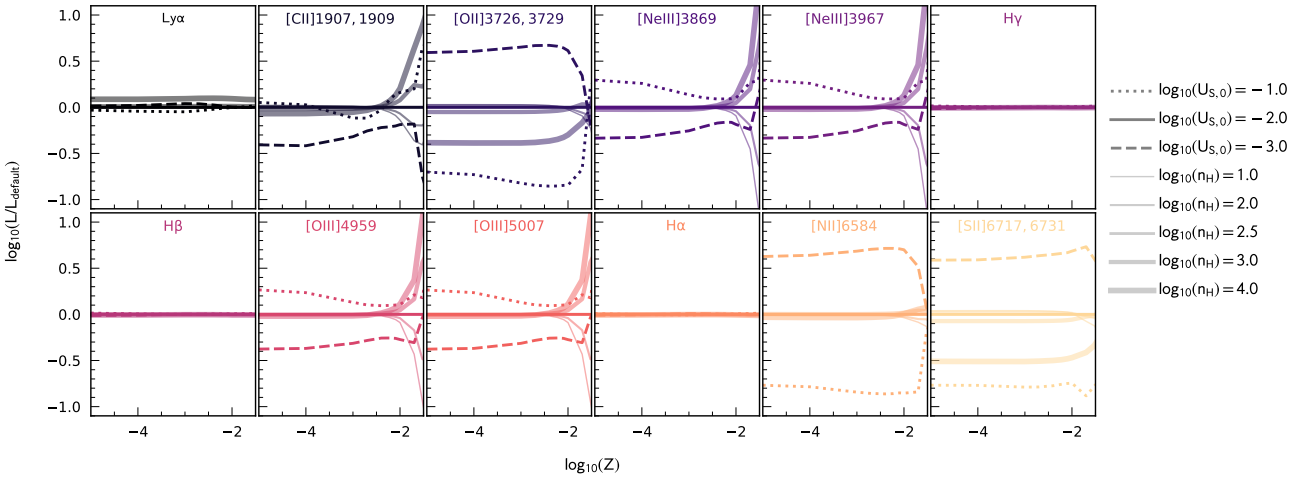

Figure A6. The effect of changing the ionisation parameter $U_{S,\mathrm{ref}}$ and hydrogen density n_H of the relative luminosity of each of the emission lines considered in this work. The default model assumes $\log_{10}(U_{S,\mathrm{ref}}) = -2$ and $\log_{10}(n_H/cm^{-3}) = 2.5$.

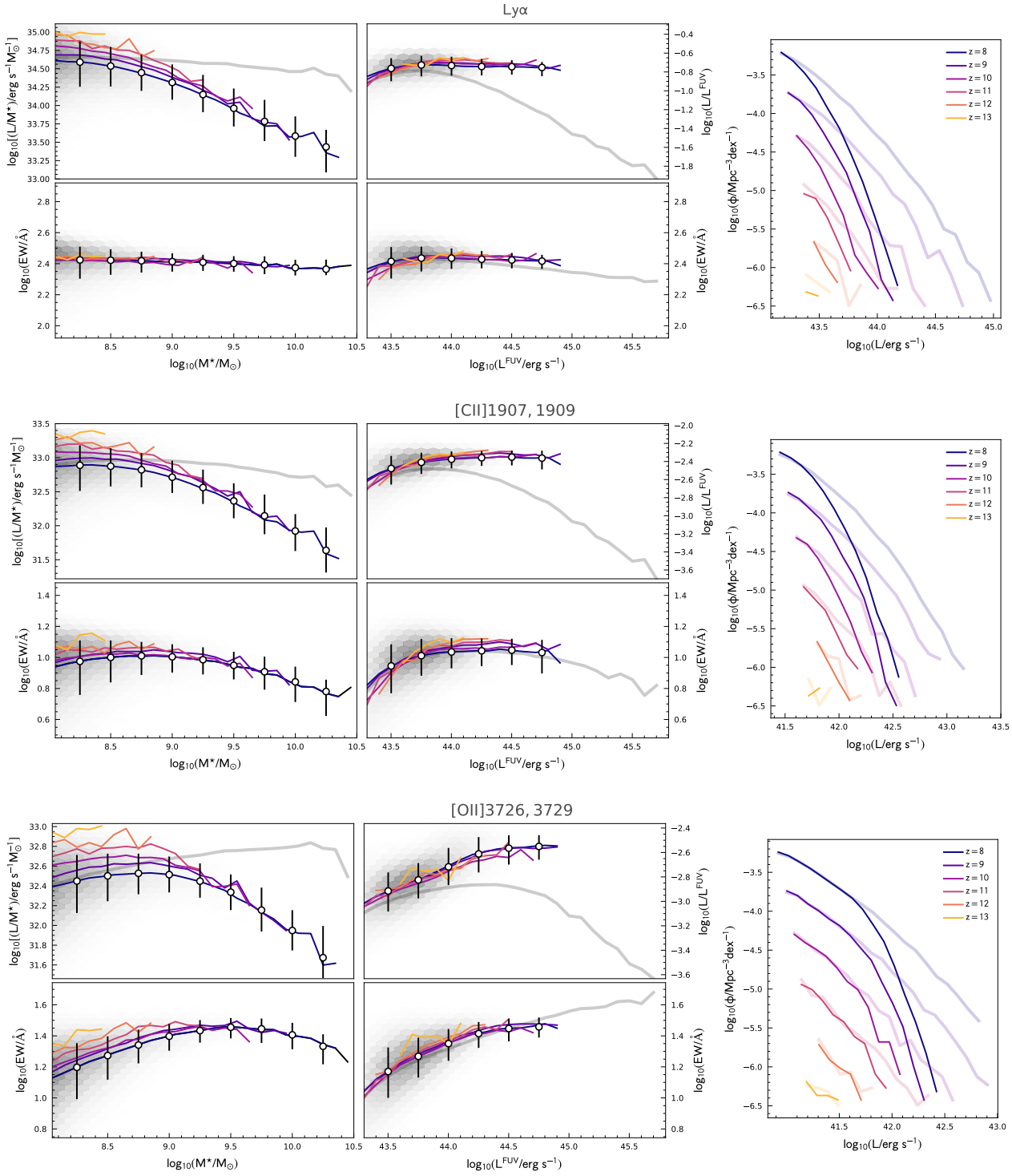

Figure B1. The relationship between line luminosity and equivalent width, and stellar mass and far-UV luminosity and line luminosity function (right-hand panels) at $z = 8 - 13$ for Lyman-α, [CIII],CIII]λ1907, 1090, and [OII]λ2726, 3729.

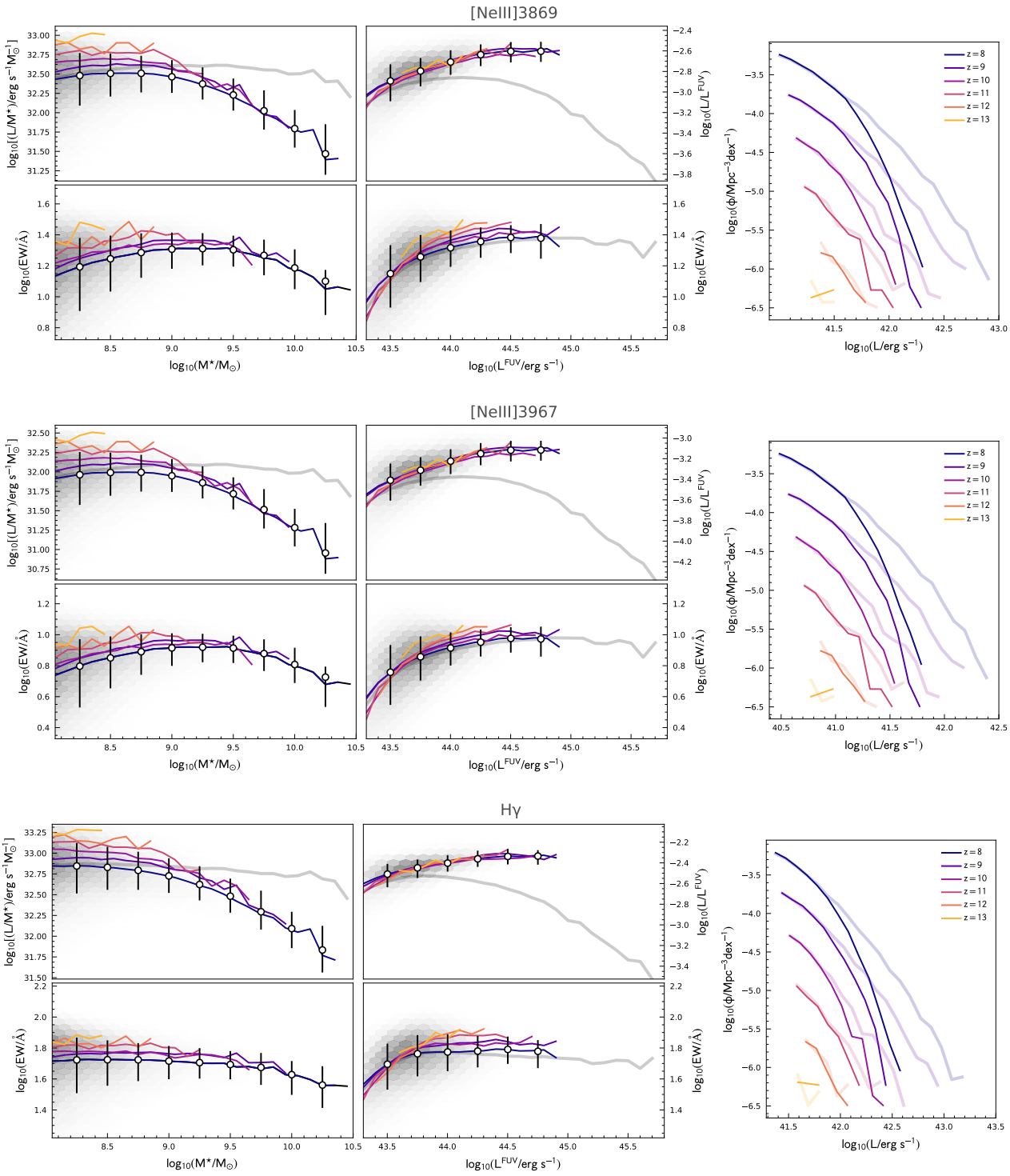

Figure B2. The same as Fig. B1 but for the [NeIII]λ3869, [NeIII]λ3967, and Hγ lines.

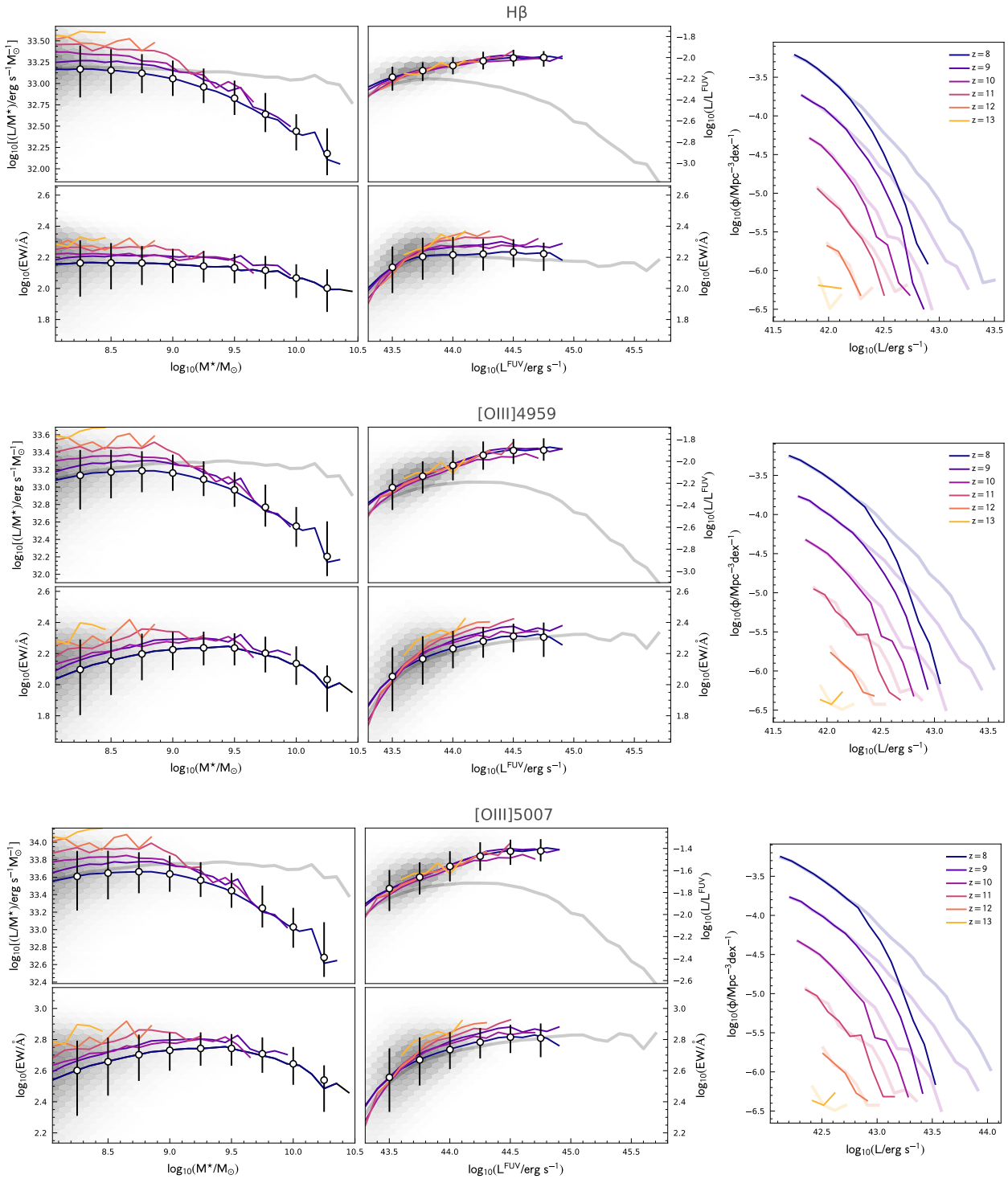

Figure B3. The same as Fig. B1 but for the Hβ, [OIII]λ4959, and [OIII]λ5007 lines.

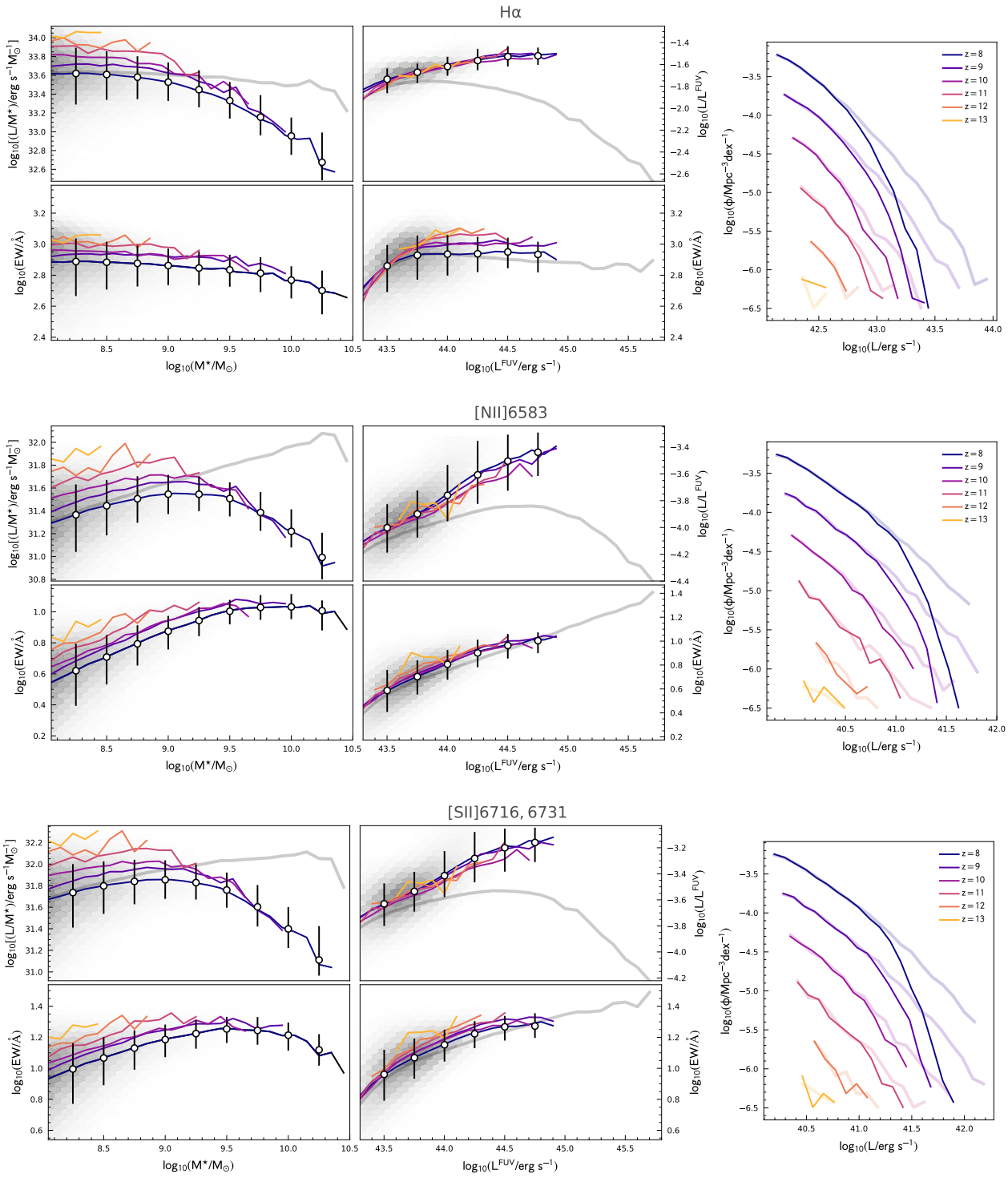

Figure B4. The same as Fig. B1 but for the Hα, [NII]λ6583, and [SII]λ6716, 6731 lines.